


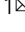



## Loop currents in two-leg ladder cuprates

Dalila Bounoua<sup>1</sup>, Lucile Mangin-Thro<sup>2</sup>, Jaehong Jeong<sup>1</sup>, Romuald Saint-Martin<sup>3</sup>, Loreynne Pinsard-Gaudart<sup>3</sup>, Yvan Sidis<sup>1</sup> & Philippe Bourges<sup>1</sup>

New phases with broken discrete Ising symmetries are uncovered in quantum materials with strong electronic correlations. The two-leg ladder cuprate  $Sr_{14-x}Ca_xCu_{24}O_{41}$  hosts a very rich phase diagram where, upon hole doping, the system exhibits a spin liquid state ending to an intriguing ordered magnetic state at larger  $Ca$  content. Using polarized neutron diffraction, we report here the existence of short range magnetism in this material for two  $Ca$  contents, whose origin cannot be ascribed to Cu spins. This magnetism develops exclusively within the two-leg ladders with a diffraction pattern at forbidden Bragg scattering, which is the hallmark of loop current-like magnetism breaking both time-reversal and parity symmetries. Our discovery shows local discrete symmetry breaking in a one dimensional spin liquid system as theoretically predicted. It further suggests that a loop current-like phase could trigger the long range magnetic order reported at larger doping in two-leg ladder cuprates.

<sup>1</sup>Laboratoire Léon Brillouin, IRAMIS/LLB, UMR12, CEA-CNRS, CEA-Saclay, 91191 Gif sur Yvette, France. <sup>2</sup>Institut Laue-Langevin, 71 avenue des martyrs, 38000 Grenoble, France. <sup>3</sup>Equipe Synthèse Propriétés et Modélisation des Matériaux, Institut de Chimie Moléculaire et des Matériaux d'Orsay, Centre National de la Recherche Scientifique UMR 8182, Université Paris-Sud, Université Paris-Saclay, 91405 Orsay, France. ✉email: [dalila.bounoua@cea.fr](mailto:dalila.bounoua@cea.fr); [philippe.bourges@cea.fr](mailto:philippe.bourges@cea.fr)

In recent years, the study of doped Mott insulators, such as superconducting (SC) cuprates<sup>1–5</sup> or iridates<sup>6</sup>, raised the question of the existence of other kinds of magnetism. Beyond conventional spin magnetism, a new form of magnetism may originate from magneto-electric loop currents (LCs)<sup>7–13</sup> or Dirac multipoles<sup>14–17</sup>. While most of these states are usually discussed for hole-doped quasi-2D transition metal oxides such as cuprates and iridates, the existence of LCs was also addressed in quasi-1D spin ladder cuprates<sup>18–20</sup>.  $\text{Sr}_{14-x}\text{Ca}_x\text{Cu}_{24}\text{O}_{41}$  is a prototype two-leg ladder system whose hole doping can be tuned by Ca for Sr substitution. This study is motivated by the recent theoretical proposal that spin liquids and topological order could be dressed with ancillary phases, such as LCs, that highlight their intrinsic nature<sup>10–12</sup>. It represents a promising candidate for LCs hunting in the context of low-dimensional spin liquids<sup>18–20</sup>.

In cuprates, the LCs are expected to develop in the  $\text{CuO}_2$  plaquettes, the building blocks of the materials. In a 3-band Hubbard model, they originate from the frustration of the electronic hopping and interaction parameters and generate staggered orbital moments within the  $\text{CuO}_2$  plaquettes. Once ordered, they are expected to preserve the lattice translational invariance ( $q = 0$  magnetism) and break time-reversal symmetry. There may exist different LCs patterns with a single  $\text{CuO}_2$  plaquette, which can further break other  $Z_2$  symmetries, such as parity and rotation. In the so-called pseudo-gap phase of SC cuprates, there are experimental evidences of a breaking of time-reversal, parity and rotation symmetries, provided by polarized neutron diffraction (PND)<sup>1–5,21–23</sup>, muon spin spectroscopy<sup>24</sup>, second harmonic generation<sup>25</sup>, torque<sup>26</sup> and optical birefringence measurements<sup>27</sup>. Further, second harmonic generation<sup>28</sup> and PND<sup>6</sup> observations in iridates provide evidence for the universality of the LCs phase in correlated electron systems such as layered oxides.

In most SC cuprates, the LC state fully develops in the  $\text{CuO}_2$  planes, yielding a 3D long-range order. In lightly doped  $\text{La}_{2-x}\text{Sr}_x\text{CuO}_4$ , known to host a spontaneous charge segregation in the form of quasi-1D charge stripes, the LC order is frustrated. As a result, the LC magnetism remains quasi-2D and at very short range<sup>3</sup>, suggesting a possible confinement of LCs within bond centered stripes, taking the form of two-leg ladders. However, the evidence for such a kind of LC-like magnetism in low-dimension remains untackled up to date and can be investigated in the model quasi-1D system  $(\text{Sr}, \text{Ca})_{14}\text{Cu}_{24}\text{O}_{41}$ .

$\text{Sr}_{14-x}\text{Ca}_x\text{Cu}_{24}\text{O}_{41}$ , hereafter SCCO- $x$ , crystallizes with an aperiodic nuclear structure consisting of an alternating stack of 1D  $\text{CuO}_2$  chains and quasi-1D  $\text{Cu}_2\text{O}_3$  two-leg ladder layers. It realizes an intrinsically hole-doped compound with an effective charge of  $2.25^+$  per Cu ion where, in the pure compound ( $x = 0$ ), holes are located within the chains subsystem. Substitution with  $\text{Ca}^{2+}$  on the  $\text{Sr}^{2+}$  site results in a charge transfer of the holes from the chains to the ladders<sup>29</sup>, due to chemical pressure. Owing to strong electronic correlations, hole doping strikingly changes the electronic properties of SCCO- $x$ , and the corresponding phase diagram includes insulating gapped spin liquid phases within the ladders ( $\Delta_{\text{gap}} \sim 32$  meV), short-range dimer antiferromagnetic orders within the chains, charge density wave in both chains and ladders, magnetic long-range order (LRO) - assumed to be antiferromagnetic (AFM) - at large Ca-content, pressure-induced superconductivity for  $x \geq 10$ , with a predicted  $d$ -wave character in one-band Hubbard model<sup>30</sup>, and even pseudogap-like behavior for  $x \geq 9$ <sup>31,32</sup>. This work addresses the issue of the existence of LCs-like magnetism in the archetypal hole-doped spin-ladders compounds, SCCO-5 and SCCO-8 with  $\sim 13$  and  $\sim 17\%$  hole doping per Cu ion respectively, according to Osafune et al.<sup>33</sup>.

Using polarized neutron diffraction, we here report a short-range magnetism in SCCO- $x$  below  $\sim 50$  K and 80 K for two Ca contents. This magnetism is associated exclusively with the two-

leg ladder layers as the diffracted magnetic intensity occurs at forbidden Bragg positions of the ladder sub-system. Its origin cannot be related to Cu spins but rather may lie in the magneto-electric loop currents, as the ones previously reported in superconducting 2D cuprates<sup>1,23</sup>. The calculated magnetic structure factors, that satisfactorily reproduce our data, correspond to two distinct loop current patterns proposed theoretically<sup>7,8,11,12</sup>. We further suggest that the long-range magnetic order reported below  $\approx 5$  K at larger doping in two-leg ladder cuprates could be induced by the observed short-range magnetism.

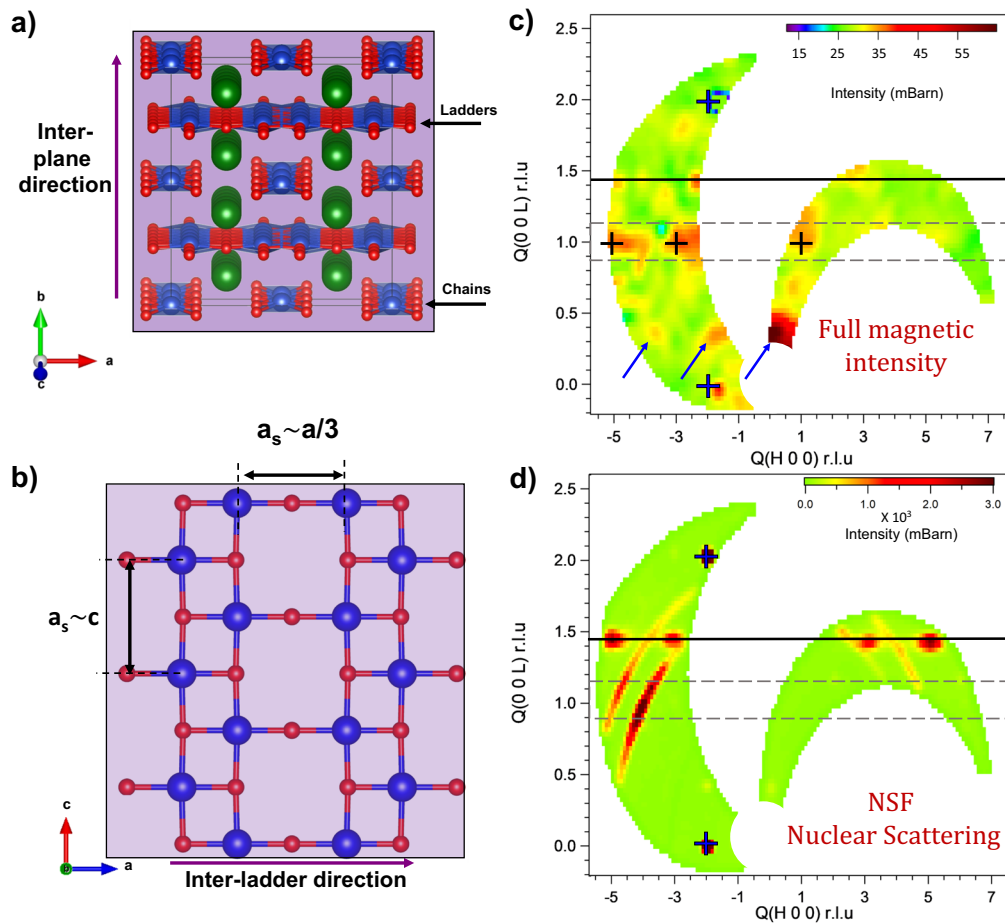
## Results

**Atomic structure.**  $\text{Sr}_{14-x}\text{Ca}_x\text{Cu}_{24}\text{O}_{41}$  exhibits an aperiodic atomic structure (shown in Fig. 1a, b) with two, chains and ladders, incommensurate sub-lattices<sup>34</sup>, which are described by the orthorhombic space groups  $A\text{mma}$  and  $F\text{mmm}$ , respectively. The crystal lattice is incommensurate along the  $c$ -axis, with an incommensurability parameter between the chains and the ladders,  $\frac{1}{\gamma} = \frac{c_{\text{ladders}}}{c_{\text{chains}}} \approx 1.43$ . Upon Ca-doping ( $x > 3$ ), the chains sub-space group changes from  $A\text{mma}$  to  $F\text{mmm}$  such that the whole structure is described using 4D crystallography in Ref. <sup>34</sup> as belonging to  $X\text{mmm}(00g)ss0$  superspace group, where  $X$  stands for nonstandard centering  $(0, 0, 0, 0)$ ,  $(0, \frac{1}{2}, \frac{1}{2}, \frac{1}{2})$ ,  $(\frac{1}{2}, \frac{1}{2}, 0, 0)$  and  $(\frac{1}{2}, 0, \frac{1}{2}, \frac{1}{2})$ . In principle, Bragg peaks need then to be indexed in the 4D superspace indexes as  $(H, K, L_{\text{ladders}}, L_{\text{chains}})$ . However, as the reported magnetism is basically related to the ladders sub-lattice, we refer through this manuscript to the Bragg positions as  $(H, K, L)$ , in units of:  $\frac{2\pi}{a} = 0.55\text{\AA}^{-1}$ ,  $\frac{2\pi}{b} = 0.48\text{\AA}^{-1}$  and  $\frac{2\pi}{c_{\text{ladders}}} = 1.61\text{\AA}^{-1}$ , with  $a = 11.4\text{\AA}$ ,  $b = 12.9\text{\AA}$  and  $c = 3.91\text{\AA}$ , where  $L_{\text{chains}} = 0$  (except where it is explicitly indicated otherwise).

Two large SCCO- $x$  single crystals have been grown (see Methods) to perform the PND experiments, which are described in more details in the Supplementary Note 1. During these experiments, SCCO- $x$  samples were aligned with the ladder sub-lattice parameters within the  $(100)/(001)$  scattering plane so that wavevectors  $\mathbf{Q}$  of the form  $(H, 0, L)$  were accessible. Wavevectors are given in reduced lattice units  $(2\pi/a, 2\pi/b, 2\pi/c)$  where  $a, b, c$  stand for the lattice parameter of the ladder subsystem ( $c$  along the legs,  $a$ , along the rungs and  $b$  perpendicular to the ladder planes  $(ac)$ , see Fig. 1a, b).

**Short-range magnetism in SCCO-8.** Figure 1c shows a  $\mathbf{Q}$ -map of the full magnetic scattering at  $T = 5$  K in SCCO-8, measured on the D7 diffractometer, extracted from longitudinal XYZ-PA (see Methods). A magnetic signal is systematically observed along  $(H, 0, 1)$  for odd integer  $H$  values and where  $L = 1$  corresponds to the ladders sublattice (crosses on Fig. 1c). These  $\mathbf{Q}$ -positions correspond to nuclear extinctions according to the atomic space group symmetry selection rules as shown by the absence of nuclear scattering at the same  $\mathbf{Q}$ -positions in the NSF channel Fig. 1d. However, the magnetic scattering appears significantly broader than the instrumental resolution, the hallmark of only short-range magnetism.

All of these results, obtained on the D7 diffractometer, are confirmed on the TAS-4F1 ( $T = 10$  K). Figure 2a shows the measured magnetic scattering, as extracted from XYZ-PA across the inter-ladder direction  $(H, 0, 1)$  in agreement with the results from D7. The  $\mathbf{Q}$ -dependence of the magnetic intensity exhibits a peculiar structure factor with the absence of scattering for  $H = 0$  and an enhanced intensity at  $H = 3$ , along the ladders scattering ridge. To better characterize this short-range magnetism (SRM), we performed scans across selected positions of the  $(H, 0, 1)$  rod. A  $L$ -scan across  $(3, 0, 1)$  position ( $SF_X$ , 4F1,  $T = 10$  K) (raw data are



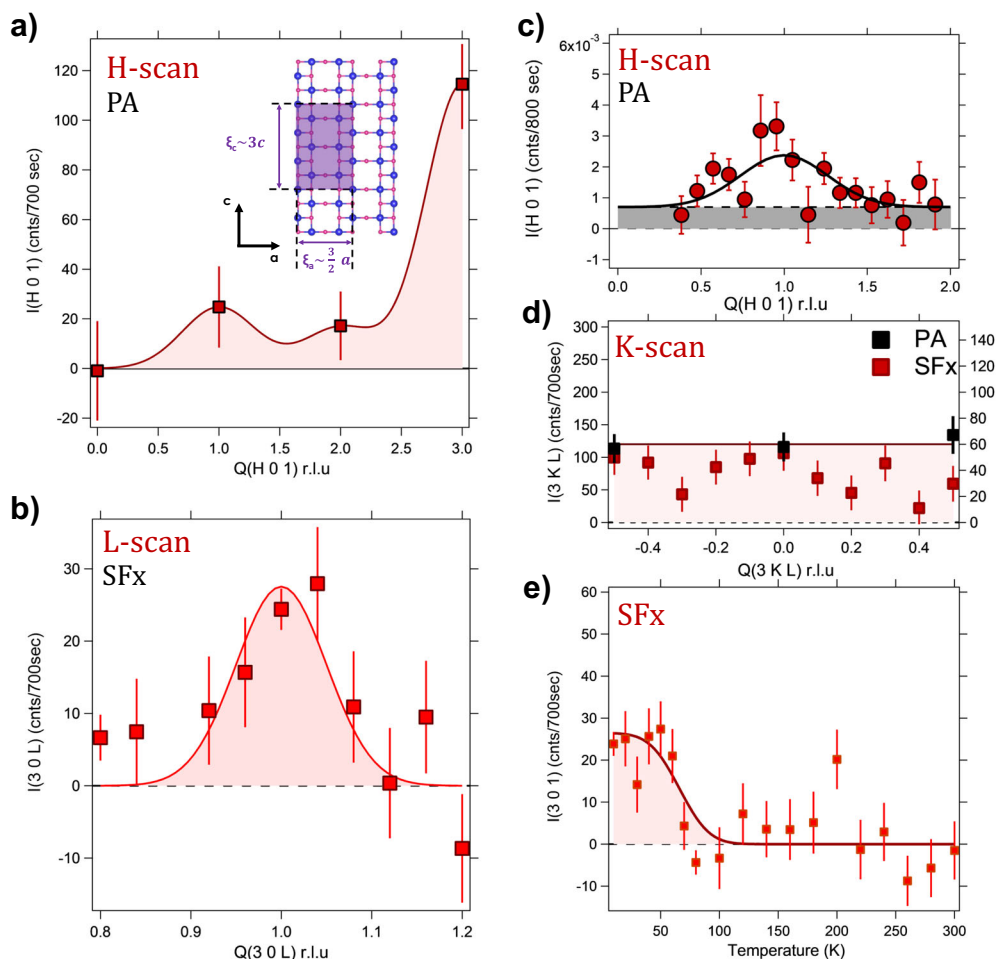
**Fig. 1** Crystal structure and magnetic map in  $\text{Sr}_6\text{Ca}_8\text{Cu}_{24}\text{O}_{41}$  sample. **a** Crystal structure of  $\text{Sr}_{14}\text{Cu}_{24}\text{O}_{41}$  showing the alternating stack of  $\text{CuO}_2$  chains (Cu in blue and O in red) and  $\text{Cu}_2\text{O}_3$  ladder planes, separated by Sr ions (in green) along the  $b$ -axis. **b**  $[a,c]$  plane projection of the ladders subsystem including one two-leg ladder. The ladders are formed by edge-sharing  $\text{CuO}_2$  squares. Mapping in momentum space of the full magnetic scattering deduced from XYZ-PA (**c**), and nuclear intensity measured in the non-spin-flip (NSF) channel (**d**) (measured on D7,  $T = 5\text{K}$ ). The maps are given in reduced lattice unit (r.l.u.) of the ladders subsystem and the intensities in mBarn. The area bounded by dashed lines indicates the ladder scattering ridge along  $(H, 0, 1)$ . The solid lines are associated with the chains nuclear response and blue crosses at integer  $H$  and  $L$  values correspond to the nuclear Bragg scattering associated with the ladders: **c** The ladders and satellite reflections magnetic spots are located by crosses and blue arrows, respectively. The magnetic satellite reflections are of the form  $(H, 0, -1, 1)$  using 4D superspace notations. In **d**, the halos correspond to aluminum powder scattering from the sample holder. Sharper red spots in **c** located at positions of strong nuclear Bragg peaks in the NSF map (**d**) are not of magnetic origin but correspond to polarization leakages from the NSF channel.

shown in Supplementary Note 2), and a  $H$ -scan across  $(1, 0, 1)$  as extracted from the D7 XYZ-PA map ( $T = 5\text{K}$ ), are reported in Fig. 2b and Fig. 2c, respectively. The scans show peaked signals with momentum widths (FWHM),  $\Delta_H = 0.5r.l.u.$  and  $\Delta_L = 0.12r.l.u.$ , which are much broader than the instrumental resolution. All along the manuscript, the correlation lengths along both directions are deduced after deconvolution from the instrument resolution, as  $\xi_a = \frac{a}{\pi\Delta_H^{dec}}$  and  $\xi_c = \frac{c}{\pi\Delta_L^{dec}}$ . The corresponding correlation lengths along the inter-ladder direction is  $\xi_a \sim 7 \pm 2.5 \text{ \AA}$  (equivalent to  $a/2$ ).  $\xi_a$  corresponds to the size of one ladder rung ( $2 \times \text{Cu-O}$  bond lengths) plus two inter-ladders spacings ( $2 \times \text{Cu-O}$  bond length) as shown in the inset of Fig. 2a.  $\xi_c$  along the ladder legs is found to be  $\xi_c \sim 11 \pm 3 \text{ \AA}$ , or correspondingly  $\sim 3c$ . The  $[a,c]$  in-plane correlation lengths are very short range and indicative of the formation of magnetic clusters within the ladders.

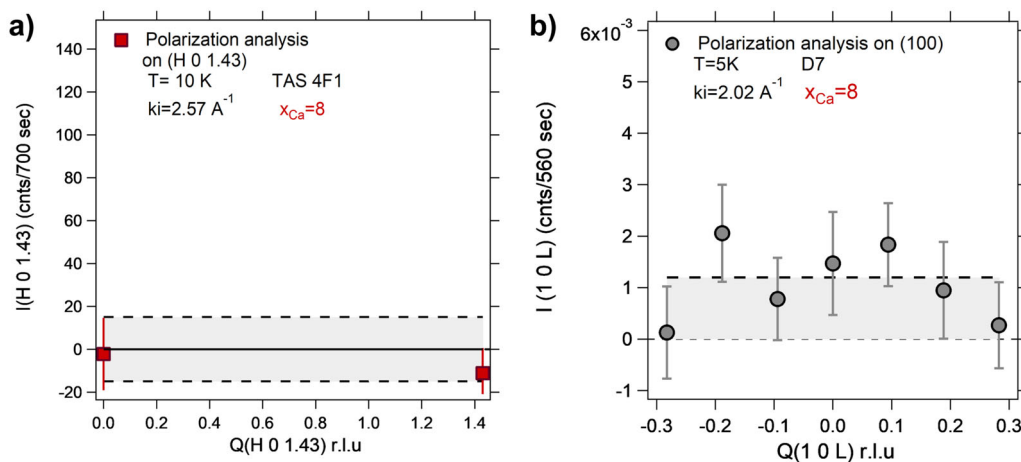
Next, we performed a survey of the  $K$ -dependence of the magnetic scattering, along the inter-planes direction (Fig. 2d). We collected a  $SF_X$  scan for a trajectory of the form  $(3, K, L)$  with  $L = 0.8$  and  $1$ . The scan at  $L = 0.8$  stands for a nonmagnetic

background according to Fig. 2b. Subtracting  $L = 0.8$  from  $L = 1$  data unveils a roughly constant level of magnetic intensity over the measured  $K$ -range, in agreement with XYZ-PA data (Fig. 2e). This indicates vanishing inter-plane correlations, emphasizing a 2D confinement of the measured magnetism within the ladder planes. The temperature dependence of the magnetic signal (Fig. 2e), measured at  $(3, 0, 1)$ , in the  $SF_X$  channel (4F1) (raw data are shown in Supplementary Note 3), shows that the magnetic correlations set-in below  $T_{mag} \sim 80 \text{ K}$ .

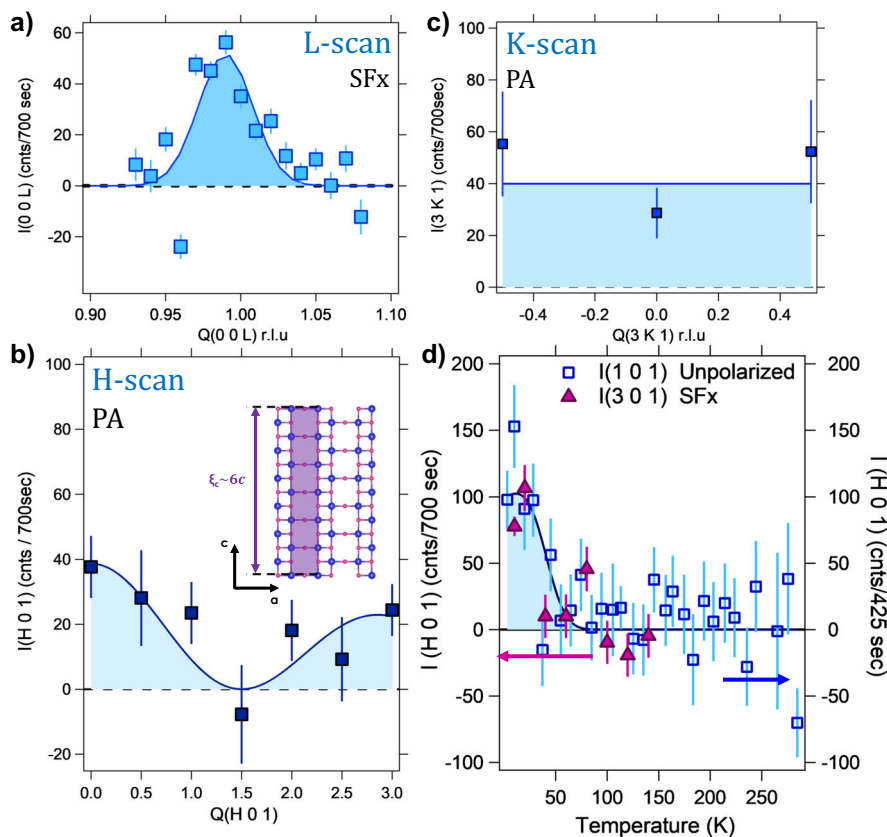
A new magnetic signal is clearly observed at  $(H, 0, L)$  with integer values of  $H$  and  $L$ , corresponding to the ladder subsystem. This raises the question of its possible existence (or fingerprint) also in the chains subsystem. In order to answer that question, one needs to look at Bragg positions  $(H, 0, 0, 1)$  using superspace notations, corresponding to  $(H, 0, 1.43)$  in the ladder subsystem units. In Fig. 1c, no magnetic intensity is sizeable at these positions. Furthermore, Fig. 3a, reporting the full scattered magnetic intensity as deduced from XYZ-PA (4F1) at two Bragg positions, shows no magnetism. That reveals the absence of any chains magnetic response at commensurate chains  $Q$ -positions. A



**Fig. 2 Magnetic scans in  $\text{Sr}_6\text{Ca}_8\text{Cu}_{24}\text{O}_{41}$ .** **a** Magnetic intensity of  $(H,0,1)$  points for integer  $H$ , i.e., along the inter-ladders direction (rungs) as extracted from XYZ polarization analysis (XYZ-PA). The inset shows real-space magnetic correlation lengths within the ladder planes. **b** Background subtracted L-scan across  $(3,0,1)$  in the spin-flip ( $SF_x$ ) channel. The magnetic intensity appears as a Gaussian signal centered at  $(3,0,1)$  (Raw data given in Supplementary Note 2). **c** H-scan across  $(1,0,1)$  direction, along the inter-ladders direction (rungs) extracted from (XYZ-PA). **d** K-scan across  $(3,0,1)$  showing the magnetic intensity along the inter-plane direction as deduced from XYZ-PA (black) and  $SF_x$  measurements after subtraction of a background intensity taken at  $(3, K, 0.8)$  (red). **e** Temperature dependence of the magnetic intensity at  $(3,0,1)$ , measured in  $SF_x$  and obtained after background subtraction (Raw data given in Supplementary Note 3). Data in **c** were measured on  $D7$  at 5 K and the others on  $4F1$  at 10 K. Lines are guide to the eye. Error bars represent one standard deviation.



**Fig. 3 Absence of magnetic signal within the chains in  $\text{Sr}_6\text{Ca}_8\text{Cu}_{24}\text{O}_{41}$ .** Full magnetic intensity deduced from XYZ polarization analysis on **(a)** ( $4F1$ ,  $T = 10$  K) within the chain subsystem along  $(H,0,0,1)$  in superspace reduced lattice unit (r.l.u.) or  $(H,0,1.43)$  in ladders r.l.u. **(b)** ( $D7$ ,  $T = 5$  K) along  $(1,0,L)$ . Error bars represent one standard deviation.



**Fig. 4** Magnetic scans in  $\text{Sr}_9\text{Ca}_5\text{Cu}_{24}\text{O}_{41}$ . **a** L-scan across  $(0,0,1)$  in the spin-flip ( $\text{SF}_x$ ) channel, showing the magnetic scattering along the ladder legs. The magnetic scattering appears as a Gaussian signal centered at  $(0,0,1)$ . (Raw data given in Supplementary Note 2). **b** H-scan of the  $(H,0,1)$  rod, the inter-ladders direction (rungs), showing the modulation of the magnetic intensity extracted from XYZ polarization analysis (XYZ-PA) (squares). The inset shows real-space magnetic correlation lengths within the ladder planes. **c** K-scan across  $(3,0,1)$  after full XYZ-PA, indicating the absence of inter-plane magnetic correlations. **d** Temperature dependence of the magnetic signal, after background subtraction (Raw data given in Supplementary Note 3). The figure combines polarized neutron data (full symbols) measured at  $(3,0,1)$  in the  $\text{SF}_x$  channel and unpolarized neutron data (open symbols) measured at  $(1,0,1)$ . All  $\mathbf{Q}$ -scans were performed on the instrument 4F1 at 10 K. Lines are guide to the eye. Error bars represent one standard deviation.

scan across the  $(1, 0, L)$  direction in SCCO-8 was also performed in order to crosscheck the absence of signal at positions of the form  $(H, 0, 0)$  (common to both ladders and chains), as shown in Fig. 3b. All scans reported in Fig. 3, emphasize that the SRM detected within the  $\text{Cu}_2\text{O}_3$  ladders is not transferred to the underlying  $\text{CuO}_2$  chain subsystem.

However, a correlated magnetic signal appears on top of satellite reflections mixing both ladders and chains subsystems, along the  $(H, 0, 0.43)$  line, with H-even (blue arrows Fig. 1c), in r.l.u. of the ladders, corresponding to the  $(H,0,-1,1)$  line in the superspace notations. That unexpected result does not necessarily mean that the chain subsystem carries magnetic moments which would be inconsistent with the absence of a magnetic signal on the chains Bragg positions. Instead, that observation suggests that the magnetic moments of the ladder could actually be magnetically coupled via the chain subsystem, leading to a non-zero magnetic structure factor at the satellite. That interpretation is in line with the inter-ladder correlations of the magnetic signal.

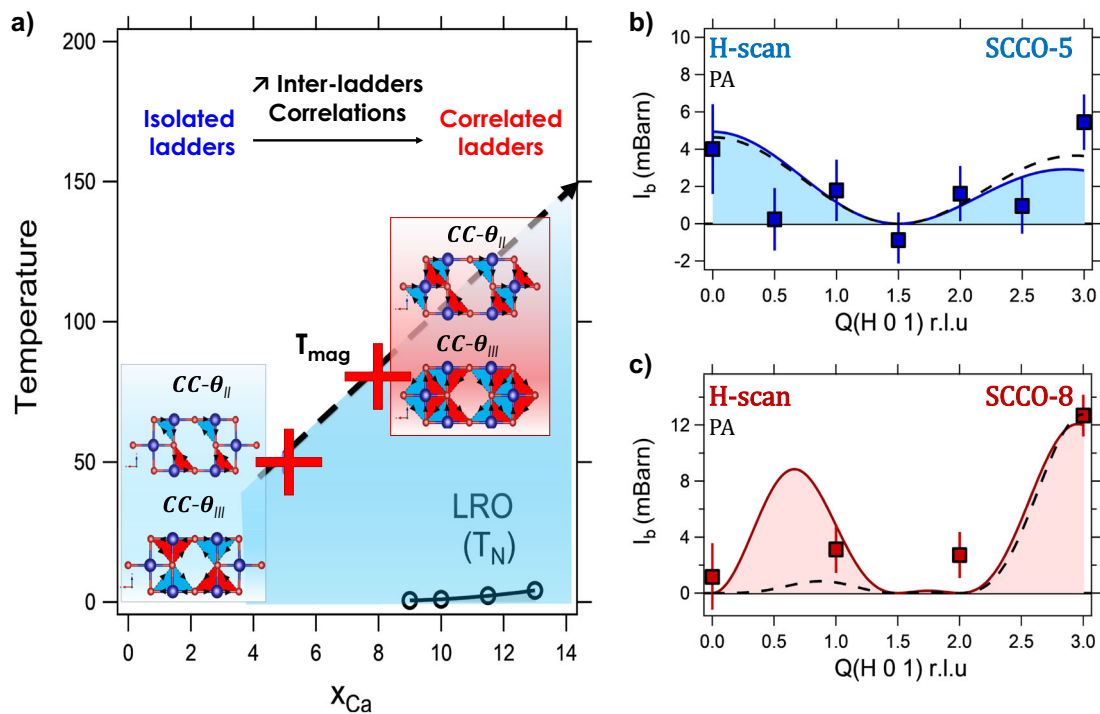
#### Lost inter-ladder correlations at lower Ca-substitution: SCCO-5.

Figure 4a shows a L-scan in the  $\text{SF}$  channel across  $(0,0,1)$  along the ladder-legs direction ( $\text{SF}_x$ , 4F1,  $T = 5\text{K}$ ), where no magnetic signal is observed for SCCO-8. The scan shows a clear magnetic signal centered at  $(0,0,1)$ , where nuclear scattering is forbidden. The FWHM of the measured signal gives (after deconvolution from the instrumental resolution) a correlation length of  $\xi_c \sim 20 \pm 6 \text{ \AA}$  along the ladders or equivalently  $\sim 6c$ , which is enhanced as

compared to the SCCO-8 compound. We further performed an XYZ-PA on 4F1 along the inter-ladder direction  $(H,0,1)$ . The XYZ-PA reported in Fig. 4b reveals a diffuse magnetic scattering along  $H$  indicating a vanishing  $\xi_c$  with only a minimum of the magnetic intensity for  $H = 1.5$ . These results highlight an even shorter-range magnetism, confined within a single ladder, and the loss of inter-ladder magnetic correlations when lowering the Ca-content. Two features, found in SCCO-8, have been similarly observed. First, the XYZ-PA along  $(3,K,1)$  reveals no maximum intensity at  $K = 0$ . In light of the results for  $x = 8$  sample (Fig. 2d), this is consistent with the absence of correlations along the  $b$ -axis (Fig. 4c), the inter-plane direction. Second, the XYZ-PA within the chains subsystem confirms the absence of chains magnetism (Supplementary Note 4). However, in contrast to SCCO-8, no magnetic intensity is observed at the satellite position corresponding to the  $(H,0,-1,1)$  line in the superspace notations, confirming the assumption that the  $\text{CuO}_2$  chain could bridge inter-ladder coupling in SCCO-8.

Figure 4d shows the temperature dependencies of the magnetic intensity at  $(3,0,1)$  and  $(1,0,1)$ , respectively (4F1). The signal at  $(3,0,1)$  was measured in the  $\text{SF}_x$  channel and corrected from a background intensity measured at  $(3,0,0.8)$ . The magnetic signal at  $(1,0,1)$  was tracked as a function of the temperature using unpolarized neutrons. Both datasets give an onset temperature  $T_{\text{mag}} \sim 50 \text{ K}$ .

Put together, all these experimental observations allow one to get a rather accurate description of the observed magnetic



**Fig. 5 Phase diagram, modelization and structure factors.** **a** Schematic phase diagram in  $\text{Sr}_{14-x}\text{Ca}_x\text{Cu}_{24}\text{O}_{41}$  (SCCO- $x$ ) showing the evolution of the loop current (LC) pattern as a function of the Ca content ( $x_{\text{Ca}}$ ). At large doping, magnetic correlations develop between ladders at the onset temperature  $T_{\text{mag}}$  (red crosses). In heavily doped samples, a magnetic long-range order (LRO) further develops below a Néel temperature  $T_N$  of a few  $\text{K}^{31}$ . Insets: **a** (top)  $\text{CC-}\theta_{\text{II}}$ <sup>7,8</sup> and (down)  $\text{CC-}\theta_{\text{III}}$ <sup>10-12</sup> models built on single ladder with two staggered Cu-O orbital currents per Cu site flowing clockwise (red triangles) and anticlockwise (blue triangles). Both models describe nicely the experimental results shown in panel **b**. **b**  $\text{CC-}\theta_{\text{II}}$  and (down)  $\text{CC-}\theta_{\text{III}}$  models with additional interladders correlations within the ladder unit cell. Both models describe nicely the experimental results shown in panel **c**. **c** H-scan of the (H,0,1) rod, the inter-ladders direction (rungs) showing the modulation of the out-of-plane magnetic intensity,  $I_b$  extracted from XYZ polarization analysis (PA) (squares) compared with magnetic structure factors deduced from 2 loop currents models, labeled  $\text{CC-}\theta_{\text{II}}$  (solid line)<sup>7,8</sup> and  $\text{CC-}\theta_{\text{III}}$  (dashed line)<sup>10-12</sup> in **b** SCCO-5 and **c** SCCO-8. Error bars represent one standard deviation.

patterns, especially thanks to the large set of collected magnetic intensities at various Q points: (i) The magnetic signal is short-range, 2D and exclusively carried by the ladder subsystems with weak inter-ladders correlations. (ii) The magnetic scattering appears on wavevectors of the form (H,0,L) with integer and odd H and L values, which are forbidden for the atomic structure due to additional symmetries of the 3D crystal structure<sup>34</sup>. That indicates that the translational invariance of the ladders sublattice is preserved with the same magnetic unit cell as the atomic one ( $q=0$  magnetism), as reported for the superconducting cuprates and iridates<sup>1,3-6</sup>, which is usually interpreted in terms of LCs. These first two points concern both Ca contents. In contrast to the SCCO-8 compound where the magnetic intensity exhibits a pronounced maximum at (3,0,1), the SRM remains confined to a single two-leg ladder for SCCO-5, as reported for the  $(\text{La}, \text{Sr})_2\text{CuO}_4$  cuprate<sup>3</sup>, with only a minimum intensity at  $H=1.5$ . Similarly, the observation of magnetic intensity at the satellite position (H,0,-1,1) differs noticeably between both Ca-concentrations inline with the loss of the inter-ladder correlations at low Ca-substitution.

**Amplitude of the SRM.** The scattering intensity can be converted in absolute units (barn), after a calibration using a reference vanadium sample (Supplementary Note 5). This leads to a full magnetic scattered intensity of  $I_{\text{mag}} \sim 28 \pm 4$  mbarn and  $I_{\text{mag}} \sim 36 \pm 15$  mbarn for SCCO-8, on 4F1 and D7 respectively, at (3, 0, 1), where the structure factor is maximum. Correspondingly, the full magnetic intensity was found to be  $I_{\text{mag}} \sim 7 \pm 2$  mbarn for SCCO-5 at the same wavevector. These amplitudes correspond to the

scattered magnetic intensity of one  $(\text{Sr}, \text{Ca})_{14}\text{Cu}_{24}\text{O}_{41}$  formula unit (f.u), namely, three  $\text{CuO}_2$  square plaquettes with 4 Cu/f.u (insets of Fig. 5a). Once normalized to a single Cu site, these amplitudes remain larger than those reported in superconducting cuprates ( $I_{\text{mag}} \sim 1-2$  mbarn per Cu)<sup>1,3,4</sup>. To date, we report the largest intensity of the SRM respecting invariance symmetry ( $q=0$ ) in cuprates.

**Orientation of the magnetic moments.** The magnitude and orientation of the measurable SRM magnetic moment  $m$  is defined as  $m^2 = m_{ac}^2 + m_b^2$ , where  $m_{ac}$  and  $m_b$  denote the ladders in-plane and out-of-plane magnetic moment, respectively (Supplementary Note 6) and  $m_{ac}^2 = m_a^2 + m_c^2$ . Both components,  $m_{ac}$  and  $m_b$ , can be derived from a full XYZ-PA but not the values  $m_a$  and  $m_c$  which are interdependent. Supposing that  $m_a = m_c$ , we reproducibly estimate the ratio  $(\frac{m_b}{m_{ac}})^2 \sim 1$  for both compounds. Consistently, 4F1 and D7 data show that 50% of the magnetic moment lies out of the ladder planes, with a tilt of the out-of-plane magnetic moment to an angle  $\Theta = \text{Atan}(\frac{m_b}{m_{ac}}) \sim 55^\circ$ . This is in agreement with previous estimates in SC cuprates where the magnetic moment associated with the LCs magnetism exhibits a similar tilt<sup>1,5,23</sup>.

## Discussion

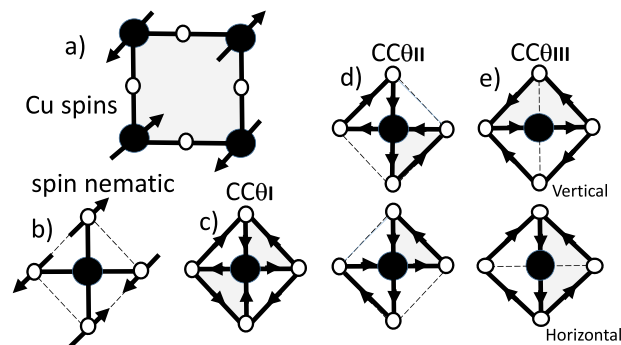
**Phase diagram.** Our experiments highlight the systematic onset of SRM within the Cu-O planes of lightly hole-doped spin ladders, with growing correlations upon increasing the hole content (Fig. 5a). We note as well the absence of a structural distortion

associated with a charge density wave instability in our samples (see Supplementary Note 7). According to magnetic susceptibility and specific heat data, no phase transition occurs in this region of the phase diagram<sup>31</sup>. However, at larger Ca doping ( $x \geq 9$ ), an AFM LRO phase is reported, but only below 4.2 K (Fig. 5a) whose antiferromagnetic nature has been basically deduced through the cusp in the temperature dependence of the macroscopic susceptibility<sup>35–38</sup>. Interestingly, the diffraction patterns of the SRM and the AFM order are located at the same wave vector in momentum space, suggesting a related origin. As the SRM occurs at higher temperature, it is tempting to propose that the reported SRM could act as a preemptive state of the AFM LRO as the Ca-doping evolution of the correlations suggests.

Meanwhile, the intrinsic nature of the AFM-LRO remains under debate as the reported locations of the magnetic Bragg peaks do not correspond to any simple model of antiferromagnetically interacting Cu spins within the ladder legs or the chains. Neutron diffraction data on single crystals indicate that the LRO involves magnetic moments both in the ladders and the chains subsystems<sup>36–38</sup> as it gives magnetic scattering at integer  $H$  and  $L$  of both ladders and chains sublattices. Therefore, complex Cu spin structures, which typically require to consider large super cells with a considerable number of independent spins, has to be invoked to describe the magnetic diffraction patterns. As recognized by Nagata et al.<sup>36,37</sup>, the model although reproducing the experimental data gives rise to an unlikely situation where the magnetic interaction between nearest-neighbor Cu spins are either ferromagnetic or antiferromagnetic and these interactions are mixed with some periodicity. Deng et al.<sup>38</sup> report two different highly non trivial magnetic structures with 96 independent spins in a large super cell (corresponding to 24 SCCO unit cells) to accommodate the measured structure factors of 36 magnetic Bragg peaks. Obviously, such a model fails to produce the SRM of SCCO-5 and 8 as the reported correlation lengths are much shorter than the super-cell size necessary to describe the complex spin structure. Additionally, the orientation of the magnetic moments in the AFM LRO phase, assumed to be related to spin moments, is found to be strictly in-plane (in the  $[a, c]$  plane) according to neutron diffraction data<sup>36,37</sup>. That contrasts with the observed SRM and suggests that both phases are distinct although related.

**Modelization.** We next propose various magnetic models that could account for the observed magnetic intensities as shown in Fig. 5b, c. One then needs to calculate the magnetic structure factor expected for given magnetic patterns. This is discussed in details in the Supplementary Note 8 for various magnetic configurations; we here recall the main conclusions. We consider various decorations of the ladder unit cell as shown in Fig. 6. Some models have been proposed theoretically, others are simplified magnetic decorations of the unit cell.

First, one considers a model of periodic antiferromagnetic Cu spins on a square lattice (Fig. 6a), that can decorate an isolated ladder. In principle, this model can be directly applied to SCCO-5 sample where one observes a magnetism confined to a single ladder. However, it completely fails to reproduce our experimental data as it breaks the translational symmetry of the lattice and would lead to SRM with scattering only at half integer  $H$  and  $L$  values at odds with our observation. For the same reason, any model built of such an AFM coupled ladder does not describe the data whatever the coupling between ladders. Neither does a model of magnetic (spin or orbital) moments on oxygen sites as considered in<sup>1,39–41</sup> (Fig. 6b). That model does respect the translation of the lattice but leads to an extinction of the structure factor at  $(3,0,1)$  where the observed intensity is maximum.



**Fig. 6 Magnetic and loop current (LC) patterns.** **a** Periodic antiferromagnetic Cu spins on a square lattice. **b** a spin (or orbital) nematic state, with two sets of staggered spin on O sites as proposed in<sup>1</sup>. **c** LC state CC- $\theta_I$ <sup>18,19</sup>. **d** LC state CC- $\theta_{II}$ <sup>8</sup> showing two possible patterns breaking rotational symmetry along the diagonals. **e** LC state CC- $\theta_{III}$ <sup>12</sup> showing Horizontal and Vertical patterns. For all models (**b–e**), the same pattern is assumed around each Cu atom on the square lattice of a single ladder.

Therefore, one is left to find out alternative models to give an explanation for the SRM and a possible link with the AFM LRO.

**Loop Currents (LCs) modeling.** In a marked contrast with highly complex magnetic arrangements of Cu spins used to describe the LRO AFM state, we propose a comprehensive interpretation of our PND measurements in the framework of LCs in two-leg ladders. Following theoretical proposals<sup>7,8,11,12</sup>, we calculate two magnetic structure factors corresponding to two distinct LCs patterns that satisfactorily reproduce our data. These two patterns are based on a set of two counter-propagating LCs per Cu site. At variance, other patterns with a set of four LCs (Fig. 6c usually referred to as CC- $\theta_I$  phase)<sup>18–20</sup> give rise to different magnetic scattering selection rules that do not satisfy the measured structure factor with extinctions at Bragg positions where the observed intensities are maximum.

**CC- $\theta_{II}$  model.** The first model consists in a CC- $\theta_{II}$  like pattern of LCs (Fig. 6d)<sup>7,8</sup> within the ladders. One needs to decorate each ladder unit cell (insets of Fig. 5a) of  $\sim 3$  Cu–O plaquettes (each plaquette has an averaged cell parameter of  $a_s = c \sim a/3$  as shown in Fig. 1b) with the two opposite LCs around each Cu atom. Note that only the out-of-plane magnetic component  $m_b$  perpendicular to the LCs,  $\equiv m_{LC}$ , can be considered for modeling<sup>22</sup>. Further, one considers equal contribution from the 4-fold degenerate domains given by a 90° rotation of LCs about the Cu-site<sup>4,8</sup>. The Cu magnetic form factor was used to fit the experimental data shown in Fig. 5b, c. Note that the data could be as well described by using an oxygen form factor (see Supplementary Note 9).

First, the model of isolated ladders with the same pattern around each Cu atom (inset A of Fig. 5a) nicely reproduces the main features of the SCCO-5 data along the  $(H,0,1)$  line (Fig. 5b) accounting for lost inter-ladder correlations. It explains also why the magnetic correlations along  $a$  (perpendicular to the ladders) are confined within a single ladder. The model gives a  $m_{LC} = 0.05 \pm 0.01\mu_B$  estimate for the magnetic moment amplitude (see Supplementary Note 10). Next, we add inter-ladder correlations which are typically imposed by the structure geometry and currents continuity as shown in the inset B of Fig. 5a. Again, the same model reasonably reproduces the data of SCCO-8 shown by Fig. 5c, with a comparable magnetic moment amplitude of  $m_{LC} = 0.05 \pm 0.01\mu_B$ . For both samples and although the magnetic cross section is larger than in superconducting cuprates, the LCs magnetic moment is of the same order of magnitude<sup>1,3–5</sup> due to

more complex magnetic structure factor with interferences related to the larger magnetic unit cell and, as well, because only  $m_b$  is here considered.

**CC- $\Theta_{III}$  model.** Next, we test the model proposed in refs. 11,12 for the case of two-dimensional spin-liquids, here labeled CC- $\Theta_{III}$  constructed from patterns shown in Fig. 6e. As for CC- $\Theta_{II}$ , there are two counter-propagating LCs, but the currents now flow only between O-sites (insets of Fig. 5a). Typically, the LCs pattern is rotated by  $45^\circ$  with respect to CC- $\Theta_{II}$ . Similarly, two orientational domains rotated by  $90^\circ$  about Cu atoms, with a two-fold degeneracy each, could be considered for this phase. However, only one orientation is found to give agreement with the experimental data along the (H,0,1) line of uncorrelated SCCO-5 (dashed line in Fig. 5b). It is the Vertical-CC- $\theta_{III}$  pattern, represented in the inset A of Fig. 5a. The Horizontal-CC- $\theta_{III}$  pattern cannot explain the measured data at  $H = 0$ . In the case of correlated ladders SCCO-8, both patterns can describe the data of Fig. 5c. The fits give good agreement to the experimental data yielding  $m_{LC}$  magnitudes of  $m_{LC} = 0.04 \pm 0.01\mu_B$  and  $m_{LC} = 0.04 \pm 0.01\mu_B$  for SCCO-8 and SCCO-5, respectively.

Interestingly, for isolated ladders, only one orientational domain of CC- $\Theta_{III}$  can account for the experimental data in contrast with the CC- $\Theta_{II}$  model which has no preferred domain orientation. In terms of the observed magnetic structure factors, magnetic dipoles (as Cu spins or moments at the oxygen sites) fail to describe our data. This is a clear indication that higher multipoles, ordered at short range, are necessary. It can correspond to anapoles (such as the LCs phases) or magnetic quadrupoles as both are intimately connected as they occur at the same level of the multipole expansion<sup>42</sup>. Both types of order parameters break both parity and time-reversal symmetries and would, in principle, cause the measured magnetism. For instance, and from purely symmetrical considerations, it is likely that models built from magneto-electric quadrupoles, as the ones proposed in 2D cuprates<sup>14,15,17</sup>, could describe the measured magnetism if proper couplings between adjacent quadrupoles in the ladder unit cell are considered. However, at present, it is unclear what type of microscopic couplings between quadrupoles would correlate adjacent ladders. We here stressed that LCs phases offer more documented microscopic models where magnetic structure factors can be readily computed.

Our report is inline with the observation of loop currents in 2D superconducting cuprates<sup>1-5</sup>. Particularly, it shows that LCs phases occur as well in 1D spin liquids systems as it has been theoretically anticipated<sup>11,12,18-20</sup>. Consistently, it is interesting to notice that short-range orbital-like magnetic order has been as well reported in  $\text{La}_{2-x}\text{Sr}_x\text{CuO}_4$  once the doped charges are confined in two-leg ladders,<sup>3</sup> bridging the occurrence of loop currents in various copper oxides. The quasi-1D structure of  $\text{Cu}_2\text{O}_3$  ladder enforces geometrical constraints that allow us to be more specific about the LCs models because the ladder unit-cell is anisotropic and it exhibits a different atomic structure. For instance, although there is an oxygen atom above Cu atoms on the ladders<sup>43</sup> at about the same distance, typically  $\sim 2.7 \text{ \AA}$ , as the apical oxygen in hole-doped mono- or bi-layer cuprates where copper is located within a  $\text{CuO}_6$  octahedron or  $\text{CuO}_5$  pyramid, the atomic structure is aperiodic and then that oxygen does not primarily belong to the same atomic sub-system than the Cu atom on the ladder. Therefore, one can consider that LCs are established only in the planar  $\text{CuO}_2$  plane, that is the first time LCs correlations are observed without apical oxygen. That point is particularly the case in the SCCO-5 sample of decorrelated ladders where no magnetic intensity occurs at the satellite

position, (0,0,-1,1), mixing both sublattices. The occurrence of LCs in a system without specific apical oxygen has stringent consequences to explain the observed tilt of the  $q = 0$  magnetism<sup>23</sup> (see Supplementary Note 11).

Both, CC- $\Theta_{II}$  and CC- $\Theta_{III}$ , LCs models that we propose capture the most salient observation of the  $\mathbf{Q}$ -dependence of the magnetic scattered intensity as reported in Fig. 5b,c whereas other models based on magnetic moments on Cu or oxygen sites fail to account for the experimental results. Note that both LCs patterns can simply be generated from a single LC orientation and considering the lattice symmetry at variance with the proposed magnetic super-cell with 96 spins to describe LRO AFM phase<sup>38</sup>. In our previous work on LSCO, the appearance of the LC-like magnetism also coincides with a net anomaly in the spin dynamics, suggesting an interplay between AFM spin correlation and LC-like electronic instability<sup>3</sup>. A similar interplay could be present in two-leg ladders, so that LC-like phase triggers at low temperature the AFM order at large Ca content. This would be consistent with a picture of a fluctuating Néel state (spin liquid state) carrying preemptive LCs orders, by analogy to the LCs order parameter resulting from the intertwining between a topological order and discrete broken symmetries in 2D spin liquids<sup>10-12</sup>.

## Methods

**Crystal growth.** We report a PND study of two SCCO- $x$  single crystals. The single crystals of  $\text{Sr}_{1-x}\text{Ca}_x\text{Cu}_2\text{O}_{41}$  with ( $x = 5$  and  $8$ ) were grown by the traveling solvent floating zone method<sup>44</sup> using a four mirror image furnace at SP2M-ICMMO. The crystals were grown from polycrystalline feed rods of the corresponding compounds, obtained by solid-state reaction of stoichiometric amounts of CuO, SrO and CaO precursors. The growth was carried out under an oxygen pressure of 5 and 8 bars for the  $x = 5$  and 8 Ca-doped  $\text{Sr}_{1-x}\text{Ca}_x\text{Cu}_2\text{O}_{41}$  respectively, in order to avoid the formation of secondary phases and favor the constrained structure resulting from Ca-doping. The growth was initiated using a solvent pellet containing 30% (Sr, Ca)O and 70% CuO and carried out with a rate of  $1 \text{ mm} \cdot \text{h}^{-1}$ . The crystals weigh 2.1 g and 2.5 g for the  $x = 5$  and 8 compositions, respectively.

**Polarized neutron diffraction.** The PND experiments of SCCO- $x$  single crystals, described in more details in the Supplementary Note 1, were carried out on two instruments: the triple-axis spectrometer (TAS) 4F1 (Orphée reactor, Saclay) and the multidetector diffractometer D7 (Institut Laue Langevin, Grenoble). These instruments are equipped with distinct neutron polarization set-ups and were operating with two distinct neutron wavelengths, to guarantee the reproducibility of the measurements. In a PND experiment, the quantization axis of the neutron spin polarization,  $\mathbf{P}$ , is given within a (X,Y,Z) Cartesian referential. For a fixed neutron spin polarization, one can selectively probe the scattered intensity in the spin-flip channel ( $SF_p$ ) where the neutron spin polarization is reversed after interaction with the sample, and the non-spin-flip channel ( $NSF_p$ ), where the neutron spin is conserved. The amount of the magnetic scattering in the  $SF_p$  channel varies as a function of the polarization  $\mathbf{P}$ . The combination of measurements in the  $SF$  channel for different  $\mathbf{P}$  is called the polarization analysis (PA). It allows a full determination of the magnetic intensity  $I_{mag}$  where the nonmagnetic background is removed.

We used incident neutron wavevectors of  $\mathbf{k}_i = 2.57 \text{ \AA}^{-1}$  on 4F1 and  $\mathbf{k}_i = 2.02 \text{ \AA}^{-1}$  on D7. The longitudinal XYZ-PA was performed using Helmholtz-like (4F1) and a quadrupolar assembly (D7) coils<sup>45</sup> allowing to choose the polarization of the neutron either along  $\mathbf{Z}$  always perpendicular to the scattering plane or along  $\mathbf{X}$  and  $\mathbf{Y}$ . The  $\mathbf{X}$  and  $\mathbf{Y}$  polarizations correspond to arbitrary directions within the scattering plane on D7, whereas  $\mathbf{X}$  is always set to be parallel to the scattering vector  $\mathbf{Q}$  on 4F1 and  $\mathbf{Y}$  is perpendicular to  $\mathbf{Q}$  but still within the scattering plane. In all experiments, the samples were aligned in the (1,0,0)/(0,0,1) scattering plane. The data are all reported in reduced lattice units (r.l.u) and the measurement procedure follows refs. 5,23.

On D7, the data were collected by performing  $\pm 10^\circ$  rocking trajectories around the (1,0,1) and (-1,0,0) positions. We then performed data reduction adapting the standard procedure<sup>46</sup>. Such scans allowed the mapping of a wide  $\mathbf{Q}$ -region spanning reflections of the form (H,0,1) and satellite reflections (H,0,0.43) in r.l.u of the ladders. Typical instrumental resolutions (full width at half maximum: FWHM) are 0.07 r.l.u. and 0.03 r.l.u. along the H and L directions, respectively. SF and NSF data were collected in the three channels X,Y,Z. All data were corrected for the flipping ratio using a quartz sample and the conversion to absolute units is done using a vanadium sample.

On 4F1, L and H-scans of the form (H,0,1) or (1,0,L) were done across reciprocal positions corresponding to the ladder scattering ridge i.e., with integer L



and H values. Typical instrumental resolutions (FWHM) are 0.1 r.l.u. and 0.04 r.l.u. along the H and L directions, respectively. Both SF and NSF scans were done in order to crosscheck the absence of nuclear scattering at magnetic positions. The PA across (H,0,1) was performed for positive and negative H-values and the corresponding intensities were then symmetrized. Our experiments also include scans along K. Such scans were performed by tilting the sample out of plane using goniometers.

### Data availability

Data collected on D7 are available at <https://doi.org/10.5291/ILL-DATA.5-53-279>. The rest of the data that support the findings of this study is available from the corresponding authors upon request.

Received: 7 April 2020; Accepted: 8 June 2020;

Published online: 07 July 2020

### References

- Fauqué, B. et al. Magnetic order in the pseudogap phase of high- $T_c$  superconductors. *Phys. Rev. Lett.* **96**, 197001 (2006).
- Li, Y. et al. Unusual magnetic order in the pseudogap region of the superconductor  $\text{HgBa}_2\text{CuO}_{4+\delta}$ . *Nature* **455**, 372 (2008).
- Balédent, V. et al. Two-dimensional orbital-like magnetic order in the high-temperature  $\text{La}_{2-x}\text{Sr}_x\text{CuO}_4$  superconductor. *Phys. Rev. Lett.* **105**, 027004 (2010).
- Bourges, P. & Sidis, Y. Novel magnetic order in the pseudogap state of high- $T_c$  copper oxides superconductors. *Comptes Rendus Phys.* **12**, 461–479 (2011).
- Mangin-Thro, L., Sidis, Y., Wildes, A. & Bourges, P. Intra-unit-cell magnetic correlations near optimal doping in  $\text{YBa}_2\text{Cu}_3\text{O}_{6.85}$ . *Nat. Commun.* **6**, 7705 (2015).
- Jeong, J., Sidis, Y., Louat, A., Brouet, V. & Bourges, P. Time-reversal symmetry breaking hidden order in  $\text{Sr}_2(\text{Ir,Rh})\text{O}_4$ . *Nat. Commun.* **8**, 15119 (2017).
- Simon, M. & Varma, C. Detection and implications of a time-reversal breaking state in underdoped cuprates. *Phys. Rev. Lett.* **89**, 247003 (2002).
- Varma, C. Theory of the pseudogap state of the cuprates. *Phys. Rev. B* **73**, 155113 (2006).
- Agterberg, D. F., Melchert, D. S. & Kashyap, M. K. Emergent loop current order from pair density wave superconductivity. *Phys. Rev. B* **91**, 054502 (2015).
- Chatterjee, S. & Sachdev, S. Insulators and metals with topological order and discrete symmetry breaking. *Phys. Rev. B* **95**, 205133 (2017).
- Chatterjee, S., Sachdev, S. & Scheurer, M. S. Intertwining topological order and broken symmetry in a theory of fluctuating spin-density waves. *Phys. Rev. Lett.* **119**, 227002 (2017).
- Scheurer, M. S. & Sachdev, S. Orbital currents in insulating and doped antiferromagnets. *Phys. Rev. B* **98**, 235126 (2018).
- Sarkar, S., Chakraborty, D. & Pépin, C. Incipient loop current order in the under-doped cuprate superconductors. *Phys. Rev. B* **100**, 214519 (2019).
- Lovesey, S., Khalyavin, D. & Van der Laan, G. Neutron diffraction and the electronic properties of  $\text{BaFe}_2\text{Se}_3$ . *Phys. Scripta* **91**, 015803 (2015).
- Lovesey, S. & Khalyavin, D. Neutron scattering by dirac multipoles. *J. Phys. Condensed Matter* **29**, 215603 (2017).
- Spaldin, N. A., Fiebig, M. & Mostovoy, M. The toroidal moment in condensed-matter physics and its relation to the magnetoelectric effect. *J. Phys. Condensed Matter* **20**, 434203 (2008).
- Fechner, M., Fierz, M. J., Thöle, F., Staub, U. & Spaldin, N. A. Quasistatic magnetoelectric multipoles as order parameter for pseudogap phase in cuprate superconductors. *Phys. Rev. B* **93**, 174419 (2016).
- Chudzinski, P., Gabay, M. & Giamarchi, T. Orbital current patterns in doped two-leg Cu-O hubbard ladders. *Phys. Rev. B* **78**, 075124 (2008).
- Chudzinski, P., Gabay, M. & Giamarchi, T. Spin rotational symmetry breaking by orbital current patterns in two-leg ladders. *Phys. Rev. B* **81**, 165402 (2010).
- Nishimoto, S., Jeckelmann, E. & Scalapino, D. Current-current correlations in the three-band model for two-leg CuO ladders: Density-matrix renormalization group study. *Phys. Rev. B* **79**, 205115 (2009).
- De Almeida-Didry, S. et al. Evidence for intra-unit-cell magnetic order in  $\text{Bi}_2\text{Sr}_2\text{CaCu}_2\text{O}_{8+\delta}$ . *Phys. Rev. B* **86**, 020504 (2012).
- Mangin-Thro, L., Li, Y., Sidis, Y. & Bourges, P. a-b anisotropy of the intra-unit-cell magnetic order in  $\text{YBa}_2\text{Cu}_3\text{O}_{6.6}$ . *Phys. Rev. Lett.* **118**, 097003 (2017).
- Tang, Y. et al. Orientation of the intra-unit-cell magnetic moment in the high- $T_c$  superconductor  $\text{HgBa}_2\text{CuO}_{4+\delta}$ . *Phys. Rev. B* **98**, 214418 (2018).
- Zhang, J. et al. Discovery of slow magnetic fluctuations and critical slowing down in the pseudogap phase of  $\text{YBa}_2\text{Cu}_3\text{O}_y$ . *Sci. Adv.* **4**, ea05235 (2018).
- Zhao, L. et al. A global inversion-symmetry-broken phase inside the pseudogap region of  $\text{YBa}_2\text{Cu}_3\text{O}_y$ . *Nat. Phys.* **13**, 250 (2017).
- Sato, Y. et al. Thermodynamic evidence for a nematic phase transition at the onset of the pseudogap in  $\text{YBa}_2\text{Cu}_3\text{O}_y$ . *Nat. Phys.* **13**, 1074 (2017).
- Lubashevsky, Y., Pan, L., Kirzhner, T., Koren, G. & Armitage, N. Optical birefringence and dichroism of cuprate superconductors in the THz regime. *Phys. Rev. Lett.* **112**, 147001 (2014).
- Zhao, L. et al. Evidence of an odd-parity hidden order in a spin-orbit coupled correlated iridate. *Nat. Phys.* **12**, 32 (2016).
- Gotoh, Y. et al. Structural modulation, hole distribution, and hole-ordered structure of the incommensurate composite crystal  $(\text{Sr}_2\text{Cu}_2\text{O}_3)_{0.70}\text{CuO}_2$ . *Phys. Rev. B* **68**, 224108 (2003).
- Faye, J. et al. d-wave superconductivity in coupled ladders. *Phys. Rev. B* **91**, 195126 (2015).
- Vuletić, T. et al. The spin-ladder and spin-chain system  $(\text{La,Y,Sr,Ca})_{1-x}\text{Cu}_2\text{O}_{41}$ : electronic phases, charge and spin dynamics. *Phys. Rep.* **428**, 169–258 (2006).
- Uehara, M. et al. Superconductivity in the ladder material  $\text{Sr}_{0.4}\text{Ca}_{13.6}\text{Cu}_{24}\text{O}_{41.84}$ . *J. Phys. Soc. Jpn* **65**, 2764–2767 (1996).
- Osafune, T., Motoyama, N., Eisaki, H. & Uchida, S. Optical study of the  $\text{Sr}_{14-x}\text{Ca}_x\text{Cu}_{24}\text{O}_{41}$  system: evidence for hole-doped  $\text{Cu}_2\text{O}_3$  ladders. *Phys. Rev. Lett.* **78**, 1980 (1997).
- Deng, G. et al. Structural evolution of one-dimensional spin-ladder compounds  $\text{Sr}_{14-x}\text{Ca}_x\text{Cu}_{24}\text{O}_{41}$  with ca doping and related evidence of hole redistribution. *Phys. Rev. B* **84**, 144111 (2011).
- Isobe, M., Uchida, Y. & Takayama-Muromachi, E. Antiferromagnetic transition in  $\text{Sr}_{14-x}\text{Ca}_x\text{Cu}_{24}\text{O}_{41}$  ( $12.5 < x < 13.6$ ) observed by magnetic measurements. *Phys. Rev. B* **59**, 8703 (1999).
- Nagata, T. et al. Antiferromagnetic ordering in the spin singlet state of the ladder/chain material:  $\text{Sr}_{2.5}\text{Ca}_{11.5}\text{Cu}_{24}\text{O}_{41}$ . *J. Phys. Soc. Jpn* **68**, 2206–2209 (1999).
- Nagata, T. et al. Antiferromagnetic ordering in the spin ladder compound;  $\text{Sr}_{14-x}\text{Ca}_x\text{Cu}_{24}\text{O}_{41}$ . *J. Phys. Soc. Jpn* **70**, 2419–2424 (2001).
- Deng, G. et al. Coexistence of long-range magnetic ordering and singlet ground state in the spin-ladder superconductor  $\text{SrCa}_{13}\text{Cu}_{24}\text{O}_{41}$ . *Phys. Rev. B* **88**, 174424 (2013).
- Sun, K., Yao, H., Fradkin, E. & Kivelson, S. A. Topological insulators and nematic phases from spontaneous symmetry breaking in 2D fermi systems with a quadratic band crossing. *Phys. Rev. Lett.* **103**, 046811 (2009).
- Fischer, M. H. & Kim, E.-A. Mean-field analysis of intra-unit-cell order in the emery model of the  $\text{CuO}_2$  plane. *Phys. Rev. B* **84**, 144502 (2011).
- Moskvin, A. Pseudogap phase in cuprates: oxygen orbital moments instead of circulating currents. *JETP Lett.* **96**, 385–390 (2012).
- Di Matteo, S. & Norman, M. Orbital currents, anapoles, and magnetic quadrupoles in  $\text{CuO}$ . *Phys. Rev. B* **85**, 235143 (2012).
- Isobe, M. & Takayama-Muromachi, E. Structural modulation and charge distribution in the spin-ladder  $\text{Ca}_{13.6}\text{Sr}_{0.4}\text{Cu}_{24+y}\text{O}_{41+z}$ . *J. Phys. Soc. Jpn* **67**, 3119–3124 (1998).
- Revcolevschi, A., Ammerahl, U. & Dhalenne, G. Crystal growth of pure and substituted low-dimensionality cuprates  $\text{CuGeO}_3$ ,  $\text{La}_2\text{CuO}_4$ ,  $\text{SrCuO}_2$ ,  $\text{SrCuO}_3$  and  $\text{Sr}_4\text{Cu}_{24}\text{O}_{41}$  by the floating zone and travelling solvent zone methods. *J. Crystal Growth* **198/199**, 593–599 (1999).
- Fennell, T., Mangin-Thro, L., Mutka, H., Nilsen, G. & Wildes, A. Wavevector and energy resolution of the polarized diffuse scattering spectrometer D7. *Nucl. Instrum. Methods Phys. Res. Section A: Accel. Spectrom. Detect. Assoc. Equip.* **857**, 24–30 (2017).
- Stewart, J. et al. Disordered materials studied using neutron polarization analysis on the multi-detector spectrometer, D7. *J. Appl. Crystallogr.* **42**, 69–84 (2009).

### Acknowledgements

The authors would like to acknowledge B. Fauqué, M. Greven, A. Goukassov, C.M. Varma and A. Wildes for fruitful discussions. We acknowledge F. Maignen and C. Meunier for their valuable technical assistance on 4F1. We acknowledge supports from the project NirvAna (contract ANR-14-OHRI-0010) of the French Agence Nationale de la Recherche (ANR). The open access fee was covered by FILL2030, a European Union project within the European Commission's Horizon 2020 Research and Innovation programme under grant agreement N°731096.

### Author contributions

Y.S. and P.B. conceived and supervised the project; D.B., Y.S. and P.B. performed the experiments at LLB Saclay with support from J.J.; D.B. and L.M.-T. performed the experiments at ILL Grenoble; D.B. and P.B. analyzed the neutron data; R.S.-M. synthesized the single crystal samples with support from L.P.-G.; D.B., Y.S. and P.B. wrote the manuscript with further contributions from all authors. All authors contributed to this work, read the manuscript and agree to its contents.

**Competing interests**

The authors declare no competing interests.

**Additional information**

**Supplementary information** is available for this paper at <https://doi.org/10.1038/s42005-020-0388-1>.

**Correspondence** and requests for materials should be addressed to D.B. or P.B.

**Reprints and permission information** is available at <http://www.nature.com/reprints>

**Publisher's note** Springer Nature remains neutral with regard to jurisdictional claims in published maps and institutional affiliations.



**Open Access** This article is licensed under a Creative Commons Attribution 4.0 International License, which permits use, sharing, adaptation, distribution and reproduction in any medium or format, as long as you give appropriate credit to the original author(s) and the source, provide a link to the Creative Commons license, and indicate if changes were made. The images or other third party material in this article are included in the article's Creative Commons license, unless indicated otherwise in a credit line to the material. If material is not included in the article's Creative Commons license and your intended use is not permitted by statutory regulation or exceeds the permitted use, you will need to obtain permission directly from the copyright holder. To view a copy of this license, visit <http://creativecommons.org/licenses/by/4.0/>.

© The Author(s) 2020